The Effect of Magmatic Activity on Hydrothermal Venting Along the Superfast-Spreading East Pacific Rise

T. Urabe,* E. T. Baker,* J. Ishibashi, R. A. Feely, K. Marumo, G. J. Massoth, A. Maruyama, K. Shitashima, K. Okamura, J. E. Lupton, A. Sonoda, T. Yamazaki, M. Aoki, J. Gendron, R. Greene, Y. Kaiho, K. Kisimoto, G. Lebon, T. Matsumoto, K. Nakamura, A. Nishizawa, O. Okano, G. Paradis, K. Roe, T. Shibata, D. Tennant, T. Vance, S. L. Walker, T. Yabuki, N. Ytow

A survey of hydrothermal activity along the superfast-spreading (approximately 150 millimeters per year) East Pacific Rise shows that hydrothermal plumes overlay approximately 60 percent of the ridge crest between 13°50′ and 18°40′S, a plume abundance nearly twice that known from any other ridge portion of comparable length. Plumes were most abundant where the axial cross section is inflated and an axial magma chamber is present. Plumes with high ratios of volatile (^3He, CH_4, and H_2S) to nonvolatile (Mn and Fe) species marked where hydrothermal circulation has been perturbed by recent magmatic activity. The high proportion of volatile-rich plumes observed implies that such episodes are more frequent here than on slower spreading ridges.

The circulation of seawater through the geothermally heated rocks of oceanic spreading ridges is the principal agent for the transfer of energy and mass between the oceanic crust and its overlying waters. This hydrothermal circulation is most concentrated at ridge axes, where episodic intrusions of magma create new ocean crust. Discharging fluids, at temperatures up to ~400°C, carry sufficient quantities of gases (for example, ^3He, H_2S, and CH_4), trace metals (for example, Fe and Mn), and other species to significantly alter oceanic geochemical budgets in many cases (*1*). These fluids rise buoyantly from the sea floor for tens to hundreds of meters, eventually forming dilute, neutrally buoyant plumes that are spread laterally by local currents (*2, 3*). Although the distribution and composition of hydrothermal discharge have been studied on slow-, intermediate-, and fast-spreading ridge segments, we have little information from superfast-spreading (>150 mm year^{-1} at the full rate) ridge segments, which are found only between ~13° and 35°S on the East Pacific Rise (EPR). Two observations in particular suggest the importance of this superfast-spreading region to the global hydrothermal budget. In 1981, Lupton and Craig (*4*) reported that an ocean-basin–scale plume of mantle-derived ^3He extended westward from the EPR at 15°S. Continued sampling of ^3He in the south Pacific has demonstrated that this plume consists of a jetlike structure with its core centered near 14°S, and that this area of the EPR provides a major fraction of the hydrothermal input to the Pacific Ocean (*3, 5*) (Fig. 1). In 1991, Detrick *et al.* (*6*) conducted the first along-axis seismic reflection survey of a superfast-spreading ridge section. This study, in conjunction with earlier seismic surveys at fast- (~120 mm year^{-1}) and intermediate- (~60 mm year^{-1}) spreading ridge sections (*7*), suggests that as the spreading rate increases, the minimum depth of the axial magma chamber (AMC) rises closer to the sea floor, presumably increasing the frequency of magmatic intrusions.

In November and December 1993, we mapped the distribution and composition of hydrothermal plumes along the EPR axis from the Garrett transform fault to ~19°S (Fig. 2). Our primary data-gathering technique was a series of seven tow-yos: continual winching of an instrument package up and down through the lowest several hundred meters of the water column as the research vessel *Melville* steamed ahead at ~3 to 4 km hour^{-1}. The package included a Sea Bird 911 conductivity-temperature-depth sensor to transmit continuous hydrographic data, a Sea Tech transmissometer and nephelometer to transmit continuous optical data, an in situ chemical sensor, and a rosette of 20 polyvinyl chloride sampling bottles for collecting discrete samples of various dissolved and particulate hydrother-

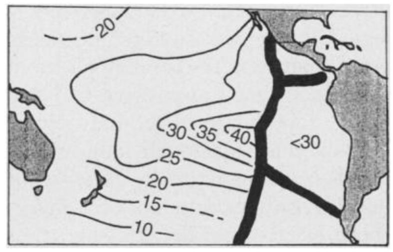

Fig. 1. Map of δ(^{3}He) percent at mid-depth (~2500 m) in the south Pacific Ocean. Data are from (*3–5*).

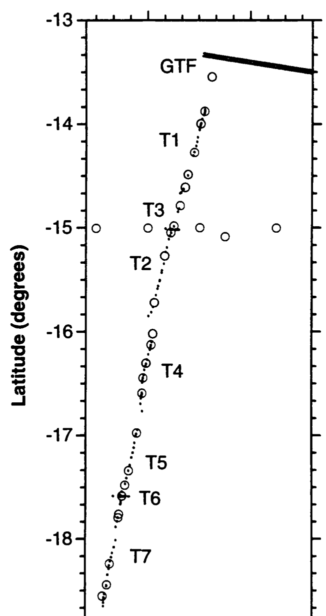

Fig. 2. Sample locations in the study area. Five continuous tow-yos (T1, T2, T4, T5, and T7) were conducted along the ridge crest and two (T3 and T6) across the crest. Twenty discrete samples were collected along each tow-yo (dots) and at each of 30 vertical cast locations (open circles). GTF, Garrett transform fault.

T. Urabe, K. Marumo, T. Yamazaki, K. Kisimoto, K. Nakamura, Geological Survey of Japan, 1-1, Higashi, Tsukuba, 305 Japan.
E. T. Baker, R. A. Feely, G. J. Massoth, G. Lebon, J. Gendron, K. Roe, D. Tennant, T. Vance, S. L. Walker, Pacific Marine Environmental Laboratory, 7600 Sand Point Way North East, Seattle, WA 98115-0070, USA.
J. Ishibashi, Laboratory for Earthquake Chemistry, Faculty of Science, University of Tokyo, Hongo, Tokyo, 113 Japan.
A. Maruyama, National Institute of Bioscience and Human Technology, 1-1, Higashi, Tsukuba, 305 Japan.
K. Shitashima, Central Research Institute of Electric Power Industry, Abiko, Abiko, Chiba, 270 Japan.
K. Okamura, Research Center for Instrumental Analyses, Kyoto University, Kitashirakawa, Kyoto, 606 Japan.
J. E. Lupton, R. Greene, G. Paradis, M. O. Hatfield Marine Science Center, Pacific Marine Environmental Laboratory, Newport, OR 97365, USA.
A. Sonoda and M. Aoki, Nippon Marine Enterprises Limited, 14, Ogawa-cho, Yokosuka, 238 Japan.
Y. Kaiho and T. Matsumoto, Japan Marine Science and Technology Center, 2-15, Natsushima, Yokosuka, 237 Japan.
A. Nishizawa and T. Yabuki, Hydrographic Department, Maritime Safety Agency of Japan, 5-3, Tsukiji, Tokyo, 104 Japan.
O. Okano and T. Shibata, Department of Earth Sciences, Okayama University, Tsushima-naka, Okayama, 700 Japan.
N. Ytow, Institute of Biological Sciences, University of Tsukuba, Tsukuba, 305 Japan.

*To whom correspondence should be addressed.

mal species. We conducted shipboard measurements of dissolved Mn, Al, and CH_4, and did x-ray fluorescence analysis of suspended particles (8). Samples were also collected for shore-based analysis of He isotopes, trace metals, nutrients, suspended particles, and microbial biomass (8). In addition to the plume survey, we collected rock samples, swath bathymetry, and underway geomagnetic vector data.

The 540-km-long survey area is distinguished by an unusually consistent axial depth of ~2650 m (Fig. 3D). The Garrett transform fault bounds the area to the north, and several second-, third-, and fourth-order discontinuities (9) tectonically and magmatically segment the axis. We use the segmentation nomenclature of Sinton *et al.* (*10*) for this region, with the addition of a subdivision of segment K. The cross-sectional width of the axis varies systematically with latitude (Fig. 3A), which suggests significant along-axis variations in the magma supply (*11*). The cross-sectional width is moderate near 14°S, steadily decreases to a minimum around the large, overlapping spreading center (OSC) at 15°55′S, and then increases to a maximum between 17° and 18°S. The continuity of the seismic reflector at the top of the AMC shows a similar latitudinal trend (6). The AMC is shallow and continuous from 13°40′ to 15°20′S, is apparently absent from 15°20′ to 16°30′S, and is mostly continuous but more variable in depth from 16°30′ to 18°50′S (Fig. 3C). Crustal magnetization was strongest at major OSCs at 15°55′, 16°30′, 17°05′, and 17°55′S (Fig. 3B). The weakest magnetization occurred at the fourth-order discontinuity at 15°S, which suggests extensive hydrothermal alteration or a high crustal temperature at that site.

Hydrothermal plumes were most readily identified by near-bottom increases in light scattering (measured by the nephelometer) and attenuation (measured by the transmissometer) produced by hydrothermally derived mineral precipitates, microbial cells, and organic debris (Fig. 3E). The trend of anomalies in the temperature field is closely congruent with that of the optical anomalies (*12*). Analytical transmission electron microscopy of filtered particles found abundant aggregates of iron oxyhydroxide composed of individual precipitates <0.01 μm in diameter. A plot of along-axis nephelometer intensity shows frequent maxima with an along-axis length scale of ~1 to 10 km, presumably corresponding to discrete patches of seafloor hydrothermal discharge (Fig. 3E). Mass concentration of particles in the plumes reached unusually high maxima of >100 μg liter^{-1}. Hydrothermal plumes were virtually continuous along the ridge axis between 17°30 and 18°40′S, which is a larg-

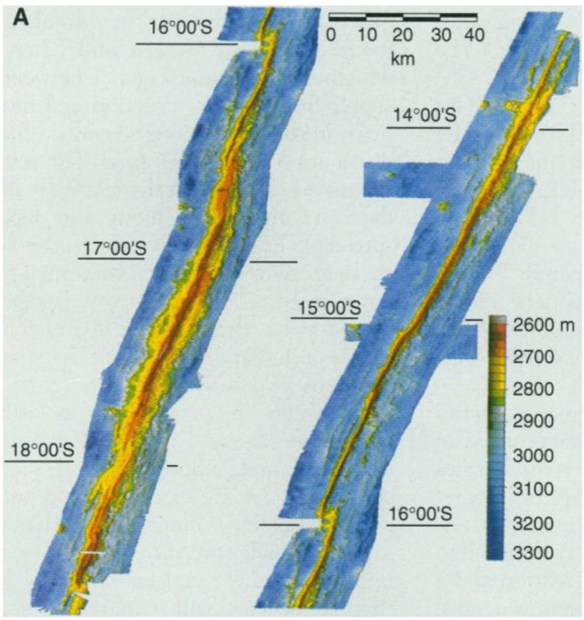

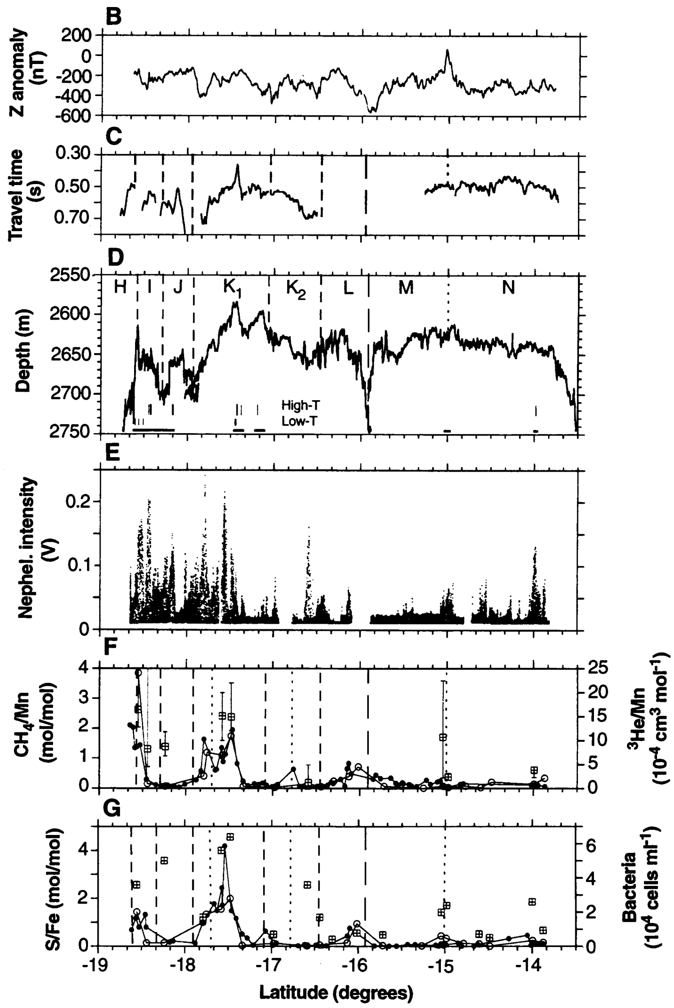

Fig. 3. Along-axis geological features and optical-chemical-biological plume indicators. (**A**) False-color rendition of ridge-crest bathymetry from a Sea-Beam 2000 swath survey. Red and yellow colors indicate depths <2900 m and illustrate latitudinal changes in axial width. Cross-axis scale has been expanded ×2 for clarity. (**B**) Relative vertical-component (Z) anomaly of the geomagnetic vector. Negative spikes in the southern hemisphere indicate strong magnetization (low crustal temperature or little hydrothermal alteration); positive spikes indicate weak magnetization (high crustal temperature or extensive alteration). (**C**) Depth (two-way travel time in seconds) to the seismic reflector at the top of the AMC (*6*). The median depth of the reflector is ~1200 m, with a minimum of <900 m at 17°26′S. (**D**) Depth of the ridge along the axis. Vertical lines above the bathymetry mark second- (long dashes), third- (short dashes), and fourth-order (dots) tectonic boundaries, as defined by (*9*) and identified here by (*10*). Vertical lines below the bathymetry give the position of high- and low-temperature discharge sites discovered by the submersible *Nautile* (*14*) in November to December 1993 and by *Shinkai 6500* in September to November 1994 (*15*). Bars beneath the discharge sites show the extent of the *Nautile* and *Shinkai 6500* surveys. (**E**) Relative nephelometer intensity (volts) from 15-s averages of all along-axis tow-yo data. About 60% of the axis produces plumes with light-scattering intensity exceeding the background value of ~0.022 V. Scale: 0.02 V ≅ 0.01 m^{-1} beam attenuation units. (**F**) Molar ratios of CH_4/Mn from tow-yo samples (dots) and plume maximum values from vertical casts (open circles). The ^{3}He/Mn [10^{-4} cm^3 mol^{-1}(STP)] mean values and range are from selected vertical casts (crosses in squares). (**G**) Molar ratios of S/Fe from tow-yo samples (dots) and plume maximum values from vertical casts (open circles). Maximum values of bacterial counts per milliliter (crosses in squares) are from vertical casts. Ambient seawater value ≅ 0.3 × 10^4 cells ml^{-1}.

er active area than observed on any other oceanic spreading center (*13*).

Coincident with our cruise, the French submersible *Nautile* conducted 23 dives in three areas: 17°08′ to 17°12′, 17°22′ to 17°28′, and 18°10′ to 18°37′S (*14*). The Japanese submersible *Shinkai* 6500 completed 25 dives in the same region, plus 5 dives farther north, in September to November 1994 (*15*). Observations in the areas around 17°25′ and 18°34′S describe clear evidence of recent eruptions. Shimmering water rose from unsedimented lavas not yet colonized by hydrothermal fauna. Temperatures in a crack in sheetlike lava approached 150°C. Between these areas lies a more tectonic regime, with abundant faults and fissures and a continuous graben several hundred meters wide and 50 m deep. A light dusting of sediment was common in this regime. Sites of high- and low-temperature discharge discovered by the *Nautile* and *Shinkai* 6500 agree closely with sites of plume maxima (Fig. 3D).

Comparison of the plume distribution with axial bathymetry and the AMC pattern reveals a first-order relation between hydrothermal activity and ridge structure. We divided the study area into three contrasting zones. Between about 13°50′ and 15°20′S, plume maxima were common, the 2900-m contours were moderately wide apart, and the AMC was continuous at a nearly uniform depth of ~0.5 s (two-way travel time). Between 15°20′ and 16°20′S, only two small plume maxima were present, the ridge width shrank to a minimum at the 15°55′ OSC, and an AMC was unobserved. South of 16°20′S, plume maxima increased in frequency and intensity, ridge width swelled to a maximum, and the AMC was distinguished by a series of shallow spikes and discontinuities [depth increases near tectonic boundaries are likely artifacts of acoustic diffraction at the edges of melt lenses (*6*)]. The AMC rose to within 800 m of the sea floor at 17°26′S (Fig. 3C), where anomalous trends in its width and depth indicate a current magmatic intrusion and the creation of new oceanic crust (*16*).

The concentration of microbial cells in the plumes was greatest in the southern half of the study area (Fig. 3G). High concentrations of CH_4 and H_2S likely fertilize the hydrothermal microbial population, increasing the plume optical anomaly, as observed at the seafloor eruption site near 9°50′N on the EPR (*17–21*). Observations with a fluorescent microscope indicated that the bacteria were mostly free-living, small rod-cocci cells rather than microbe-rich, large amorphous particles (*22*).

We characterized the hydrothermal composition of the plumes by three tracers: CH_4/dissolved Mn, ^3He/dissolved Mn, and particulate S/particulate Fe (Fig. 3, F and G). Each ratio compares a particular volatile species [CH_4, ^3He, and S (*23*)] with that of a nonvolatile species (Mn and Fe). In general, CH_4/Mn, S/Fe, and ^3He/Mn ratios varied in concert, which is in agreement with results from (*17*). Investigations at eruption sites on other ridges indicate that a shallow magmatic intrusion immediately produces hydrothermal discharge with elevated concentrations of volatiles derived from magma degassing or phase separation of hydrothermal fluids (*24, 25*). These enrichments may last months or years, eventually evolving to a more mature circulation system with a lower concentration of volatiles (*24–26*).

These ratios describe a coherent along-axis pattern that differed significantly from the intensity pattern of the plumes themselves (Fig. 3). Throughout the survey region, high ratios arose from increases in volatile species rather than decreases in trace metal concentration. High ratios were clustered only near 17°30′ to 17°50′ and 18°30′S. A narrow zone of intermediate ratios occurred near 16°10′S. Maximum ratios in these areas ranged from 2 to 4 for CH_4/Mn and S/Fe, and from 10×10^{-4} cm^3 mol^{-1} to 16×10^{-4} cm^3 mol^{-1} [at standard temperature and pressure (STP)] for ^3He/Mn. These ratios are 3 to 10 times higher than ratios typical of vent fields not recently perturbed by magmatic activity (*17, 20, 21, 27*). Everywhere else in our survey, nonvolatile species dominated the plumes. The ratios thus define a two-component plume population: those with compositions reflecting recent magmatic activity and those with more evolved compositions.

Our study shows that magmatic activity affects the distribution and composition of hydrothermal discharge over spatial scales ranging from a few to hundreds of kilometers. At the broadest scale, regions of enhanced hydrothermal activity correspond to regions of inflated ridge cross-section and a shallow AMC. This trend confirms a similar conclusion based on a hydrothermal plume survey over the northern EPR between 8°40′ and 11°50′N (*17, 19*). On a finer scale, volatile-rich plumes in segments K_1 and I overlay sites of recent magmatic activity as indicated by the anomalously shallow AMC reflector at 17°26′S (*16*) and by lava flows from apparently recent seafloor eruptions (*14, 15*). The chemistry of plumes overlaying adjacent segments reflected evolved hydrothermal circulation with a low volatile concentration. The observations describe hydrothermal discharge that has been compositionally altered by the addition of volatiles from magma degassing and phase separation. The distribution of volatile-rich plumes suggests that seafloor-spreading episodes are segment specific and most recently occurred within segments K_1 and I. Although the peak CH_4/Mn, S/Fe, and ^3He/Mn ratios in segments K_1 and I were significantly elevated relative to those of other nearby segments, they were ~50% less than maxima measured in the plume over the 9°50′N EPR site 6 months after a seafloor lava eruption (*17, 19–21*). By comparison, H_2S concentrations in vent fluids at the 9°50′N EPR site declined ~70% in the first year after eruption (*25*). On the basis of the consistent level of enrichment in all three ratios, we speculate that either magmatic intrusions in these areas occurred at least several months before our survey or that any very recent intrusion was small and unable to sustain a prolonged period of volatile-enriched discharge.

Surveys of the AMC here (*6*) and on the northern EPR (*28*) reveal that neither axial structure, the size of crustal magma bodies, nor the volume of extrusive lava varies significantly with spreading rate. However, the average depth of the AMC was found to decrease with increasing spreading rate. This observation agrees with the crustal thermal model of Phipps Morgan and Chen (*29*), which uses a dynamic balance between heat supply from magma injection and heat loss by hydrothermal cooling to control the melt distribution within the crust. The results of our survey suggest that the relatively shallow depth of the AMC along the superfast-spreading EPR strongly affects the hydrothermal environment. Hydrothermal plumes cover about 60% of the surveyed ridge crest, almost twice the coverage found during a survey of similar extent on the fast-spreading northern EPR (*19*). Furthermore, the relatively high proportion of volatile-rich plumes we observed implies that magmatic intrusions and eruptions on a superfast-spreading ridge are more frequent, and thus perhaps smaller volumetrically, than those on more slowly spreading ridges. The calculation of credible budgets for many hydrothermal species will require an accurate global estimate of the extent and duration of hydrothermal discharge alteration by shallow magmatic intrusions.

REFERENCES AND NOTES

1. G. Thompson, in *Chemical Oceanography*, J. P. Riley and R. Chester, Eds. (Academic Press, London, 1983), vol. 8, chap. 47.
2. J. E. Lupton, J. R. Delaney, H. P. Johnson, M. K. Tivey, *Nature* **316**, 621 (1985); E. T. Baker and G. J. Massoth, *Earth Planet. Sci. Lett.* **85**, 59 (1987).
3. J. E. Lupton, in *Physical, Chemical, Biological, and Geological Interactions Within Hydrothermal Systems*, S. Humphris, L. Mullineaux, R. Zierenberg, R. Thomson, Eds. (Geophysical Monograph, American Geophysical Union, Washington, DC, in press).
4. J. E. Lupton and H. Craig, *Science* **214**, 13 (1981).
5. H. S. Ostlund, H. Craig, W. S. Broecker, D. Spencer, *Geosecs Atlantic, Pacific, and Indian Ocean Expeditions* (National Science Foundation, Washington, DC, 1987), vol. 7.
6. R. S. Detrick *et al.*, *Science* **259**, 499 (1993).
7. G. M. Purdy, L. S. L. Kong, G. L. Christeson, S. C.

Solomon, *Nature* **355**, 815 (1992).

8. Methane was stripped from seawater in a cooled charcoal trap, and its concentration was determined on a gas chromatograph with a flame ionization detector (reproducibility = 5%). Manganese concentration was measured with a chemiluminescence technique (reproducibility better than 1%) [E. Nakayama, K. Isshiki, Y. Sohrin, H. Karatani, *Anal. Chem.* **61**, 1392 (1989)]. Particulate elemental chemistry was determined by thin-film x-ray fluorescence [R. A. Feely, G. J. Massoth, G. T. Lebon, in *Marine Particles: Analysis and Characterization*, D. C. Hurd and D. W. Spencer, Eds. (Geophysical Monograph 63, American Geophysical Union, Washington, DC, 1991), pp. 251–257]. Helium isotope measurements were made on a 21-cm-radius, dual-collector, statically operated mass spectrometer, with a precision of 0.25% (1σ) in $\delta(^3He)\%$, the percentage deviation of the $^3He/^4He$ ratio from the ratio in air. Microbial cells were filtered onto glass fiber filters with a pore size of 0.2 μ and fixed in glutaraldehyde.
9. K. C. Macdonald, D. S. Scheirer, S. M. Carbotte, *Science* **253**, 986 (1991).
10. J. M. Sinton, S. M. Smaglik, J. J. Mahoney, K. C. Macdonald, *J. Geophys. Res.* **96**, 6133 (1991).
11. D. S. Scheirer and K. C. Macdonald, *ibid.* **98**, 7871 (1993).
12. E. T. Baker and T. Urabe, in preparation.
13. E. T. Baker, C. R. German, H. Elderfield, in *Physical, Chemical, Biological, and Geological Interactions Within Hydrothermal Systems*, S. Humphris, L. Mullineaux, R. Zierenberg, R. Thomson, Eds. (Geophysical Monograph, American Geophysical Union, Washington, DC, in press).
14. J.-M. Auzende *et al.*, *C. R. Acad. Sci. Paris* **319**, series II, 811 (1994); J.-M. Auzende *et al.*, *Eos* **75**, 601 (1994).
15. K. Fujioka and T. Urabe, unpublished material.
16. J. C. Mutter *et al.*, *Science* **268**, 391 (1995).
17. J. E. Lupton *et al.*, *Geophys. Res. Lett.* **20**, 2913 (1993).
18. R. M. Haymon *et al.*, *Earth Planet. Sci. Lett.* **119**, 85 (1993).
19. E. T. Baker *et al.*, *ibid.* **128**, 1 (1994).
20. R. A. Feely, J. F. Gendron, E. T. Baker, G. T. Lebon, *ibid.*, p. 19.
21. M. J. Mottl *et al.*, *Geochim. Cosmochim. Acta*, in press.
22. D. M. Karl, C. O. Wirsen, H. W. Jannasch, *Science* **207**, 1345 (1980); A. Maruyama *et al.*, *J. Oceanogr.* **49**, 353 (1993).
23. The enrichment of S in hydrothermal plume particles results from precipitation of S-bearing phases from vent fluids strongly enriched in volatile H_2S.
24. E. T. Baker and J. E. Lupton, *Nature* **346**, 556 (1990).
25. K. L. Von Damm *et al.*, *ibid.* **375**, 47 (1995).
26. D. A. Butterfield and G. J. Massoth, *J. Geophys. Res.* **99**, 4951 (1994).
27. G. J. Massoth *et al.*, *ibid.*, p. 4905; T. Gamo *et al.*, *Deep-Sea Res.* **40**, 2335 (1993); C. R. German *et al.*, *Earth Planet. Sci. Lett.* **121**, 647 (1994).
28. R. S. Detrick *et al.*, *Nature* **326**, 35 (1987).
29. J. Phipps Morgan and Y. J. Chen, *ibid.* **364**, 706 (1993).

30. Funded by the Ridge Flux Project of the Science and Technology Agency of Japan and by the VENTS Program of the National Oceanic and Atmospheric Administration.

27 March 1995; accepted 19 June 1995

Catalysis of the Olivine to Spinel Transformation by High Clinoenstatite

T. G. Sharp* and D. C. Rubie

Although enstatite is a major constituent of the Earth's upper mantle and subducting lithosphere, most kinetic studies of olivine phase transformations have typically involved single-phase polycrystalline aggregates. Transmission electron microscopy investigations of olivine to spinel and modified spinel (β phase) reactions in the $(Mg,Fe)_2SiO_4$-$(Mg,Fe)SiO_3$ system show that transformation of olivine in the stability field of spinel plus β phase begins with coherent nucleation of spinel on high-clinoenstatite grains. These observations demonstrate that high clinoenstatite can catalyze the transformation by enhancing nucleation kinetics and therefore imply that secondary phases can influence reaction kinetics during high-pressure mineral transformations.

Seismic discontinuities in the Earth's mantle are generally believed to be caused by high-pressure phase transformations, with a possible additional contribution from compositional stratification (*1–3*). The 410-km and 660-km discontinuities, for example, define the Earth's transition zone and are correlated with, respectively, the transformation of $(Mg,Fe)_2SiO_4$ olivine to $(Mg,Fe)_2SiO_4$ β phase and of $(Mg,Fe)_2SiO_4$ spinel to $(Mg,Fe)SiO_3$ perovskite + $(Mg,Fe)O$ magnesiowüstite. Recent seismic data suggest that these mantle discontinuities are thinner than predicted from the equilibrium phase diagrams for adiabatic geotherms (*4*). Solomatov and Stevenson (*5*) have recently argued that the sharpness of the 410-km and 660-km discontinuities may be a result of sluggish reaction kinetics and nonequilibrium phase transformations as material convects across the phase boundary. The key parameter in their kinetic model is the nucleation rate and, in particular, the depth (that is, pressure) to which an equilibrium phase boundary can be overstepped before nucleation occurs. Similarly, in subduction zones, the depth to which olivine can be transported before it transforms into its more dense polymorphs is also controlled by reaction kinetics (*6, 7*). In this case, nucleation kinetics are especially important in relatively warm subduction zones and the warmer regions of cold subducting slabs (*7*). Nucleation can be the rate-controlling step during metamorphic reactions in the Earth's crust (*8*) and can result in the crystallization of nonequilibrium mineral assemblages (*9*).

Theoretically, nucleation kinetics are sensitive to both the strain energy and interfacial energy that accompany nucleation (*5, 10, 11*). Both of these parameters are poorly constrained for mineralogical reactions largely because of the limited number of experimental studies of nucleation kinetics (*11, 12*). For simplicity, nucleation during high-pressure polymorphic mineral transformations has generally been studied experimentally in single-phase polycrystalline aggregates (*11–13*). We demonstrate here, however, that in the case of the olivine-spinel transformation, the presence of clinoenstatite has a strong effect on the kinetics of spinel nucleation.

We performed experiments at high pressure and temperature using a multianvil apparatus (*14*) with a starting material consisting of powdered San Carlos olivine ($Mg_{1.8}Fe_{0.2}SiO_4$) plus a few percent of Mg-rich orthopyroxene. Each experiment consisted of two stages: (i) hot pressing in the stability field of olivine + high clinoenstatite at 1523 K and 10 to 11 GPa for 2.5 to 3.0 hours and (ii) reaction to high-pressure phases at 1173 to 1273 K and 14 to 15 GPa for up to 12 hours. For the olivine component, these latter conditions lie in the stability field (Fig. 1) of either β phase or β phase + spinel (*15*). Between the hot-pressing and transformation stages, the temperature was reduced to 873 K to prevent transformation during the second compression.

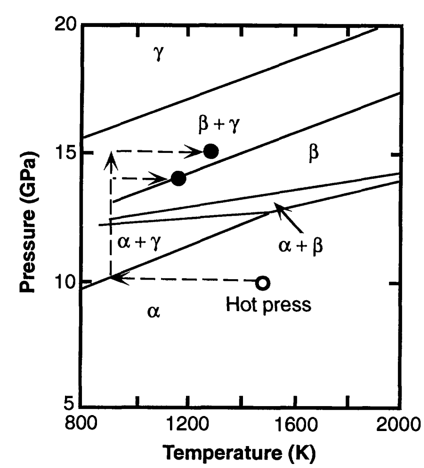

Fig. 1. Phase diagram for the $(Mg_{1.8}Fe_{0.2})_2SiO_4$ system (*15*) showing the experimental run conditions. The open circle represents the hot-pressing conditions and the solid circles show the transformation conditions. The arrows represent the paths followed from hot pressing to the transformation conditions. The stability fields are labeled as α (olivine), β (β phase), or γ (spinel).

Bayerisches Geoinstitut, Universität Bayreuth, D-95440 Bayreuth, Germany.

*To whom correspondence should be addressed.